HIGH-FIDELITY AERO-STRUCTURAL OPTIMIZATION OF THE WING TWIST USING THE NASA COMMON RESEARCH MODEL

J. M. Feldwisch, T. Klimmek,
Dep. Loads Analysis and Aeroelastic Design, DLR Institute of Aeroelasticity,
Bunsenstraße 10, 37073 Göttingen
S. Keye,
Dep. Transport Aircraft, DLR Institute of Aerodynamics and Flow Technology,
Lilienthalplatz 7, 38108 Braunschweig

Abstract

Gradient-based aero-structural optimization strategies using high-fidelity CFD methods and close-to-reality structural simulation models for the complete aircraft are promising concepts for multidisciplinary optimization (MDO) in view of new aircraft configurations. At DLR such an MDO process has been implemented for the NASA Common Research Model (CRM), a generic wide body aircraft configuration. The process capabilities have been demonstrated by optimizing the outer wing geometry including the engine. The structural optimization of the wingbox is done at each step of the aerodynamic optimization. A further development is provided in the present paper by computing and integrating design sensitivities of the structural discipline at system level. The performance of the CRM is evaluated at Ma=0.85 by solving the Reynolds-averaged-Navier-Stokes (RANS) equations, which are coupled iteratively with a structural model of the complete aircraft. The trimmed $1g$ cruise flight is achieved by adjusting the angle-of-attack and the elevator. The corresponding structural finite element model is generated and all involved simulation models are set up using a parametric approach. Aeroelastic loads are calculated by MSC Nastran for selected load cases that are assumed to be representative for the design loads. The load carrying structural components are then sized with the calculated loads. The structural process can be treated as a black box. High-fidelity, aerodynamic performance gradients with respect to a parameterized wing twist distribution are computed using the adjoint method. Structural gradients are determined by finite differences of the structural design process. Minimizing the product of the maximum root bending moment from the loads analysis and the drag coefficient shows to reduce the wing's structural mass by $-12.22\,\%$ but also lowers the aerodynamic performance by $-8.31\,\%$. A Breguet based range optimization improves the aerodynamic performance by $0.7\,\%$ and increases the wing's structural mass by $2\,\%$.

NOMENCLATURE

CFD	Computational fluid dynamics
CRM	Common Research Model
CSM	Computational structural mechanics
CWB	Center wingbox
EAS	Equivalent air speed
FD	Finite difference
FE	Finite elements
FFD	Free-Form Deformation
HTP	Horizontal tail plane
KS	Kreisselmeier Steinhauser
LRA	Load reference axis
MAC	Mean aerodynamic chord
MDO	Multidisciplinary optimization
ModGen	Model generator
MoNa	Loads and Structural design process
RANS	Reynolds averaged Navier-Stokes
SQP	Sequential Quadratic Programming
VLM	Vortex lattice method
VMM	Variable Metric Method
VTP	Vertical tail plane
α	Angle of attack
$\eta = \frac{2y}{b}$	Normalized span coordinate
Λ_{25}	Sweep
ρ	Density
Θ	Twist angle
ξ	Elevator deflection
$\bar{q}$	Dynamic pressure
$\boldsymbol{x}_a, x_{a,i}$	Aerodynamic design variables
b	Wing span
C	Chord
C_D	Drag coefficient
C_L	Lift coefficient
C_{my}	Pitch moment coefficient
f	Response function
H	Altitude
m_{F}	Fuel mass
m_{TO}	Take off mass
m_{WS}	Half wingbox structural mass
M_x^{LRA}	Bending moment
Ma	Mach number
R	Range factor
S_{ref}	Wing area
V	Speed

1 INTRODUCTION

MDO is still a field of intense research because it is believed to find better solutions compared to a sequential design approach. A sound MDO framework could reduce the development time and the risk of bad design decisions. Such decisions in the early design phase could cause an infeasible design after detailed investigation. Late fixes are expected to be expensive or to reduce the product performance.

Moreover research organizations and universities undertake efforts to uncover the unused potential of modern aircraft and

doi:10.25967/480061

even to determine a sound design for unconventional configurations. The common disciplines in published MDO studies of recent years are aerodynamics, weight estimations and structural analysis (occurrence in descending order) [1].

For each of the disciplines, analysis methods of different levels of fidelity can be utilized. Aerodynamic methods are either subsonic and invsicid panel methods [2, 3], inviscid Euler CFD methods [4, 5] or Reynolds averaged Navier-Stokes CFD methods [6–9]. Depending on the optimization problem and process definition, multiple levels of fidelity are used for the same discipline. In [9], the VLM is used to compute the design loads and the RANS equations are solved to evaluate the cruise flight performance. In another study [3], a VLM is utilized but the responses are calibrated by results from 2D CFD computations at selected sections.

Also, methods and models with different levels of fidelity are utilized for the structural analysis. Equivalent beam models are used for some aeroelastic computations [7, 10]. If they are set up carefully, elastic deflections can be captured well enough. Finite element shell structures allow more complex geometries and provide stress values which can also be used for buckling analysis. While some studies use only shell structures [11, 12], other studies use also beam elements to represent stringers and stiffeners [2, 9, 13] and are therefore closer to reality.

To achieve more realistic aerodynamic models, complete aircraft configurations are used in several MDO studies [5, 8, 14–17]. Often, an elastic model for the wing is considered and the elastic effects of the fuselage and the tail planes are neglected [7, 8, 11]. Complete aircraft configuration models (fuselage, wing, HTP, engine) have been used for both, structures and aerodynamics, in a recent high-fidelity study at DLR [9].

In general, various gradient free and gradient based optimization methods are available options. Since gradient based approaches may need less function evaluations, they are more likely to be used for MDO with computationally expensive high-fidelity methods. However, the gradients need to be determined as well, which can become computationally expensive. Finite differences (FD) schemes can be derived from a Taylor approximation of the nonlinear equations. As the computational costs scale with the number of design variables, FD is only efficient if the number of responses is larger than the number of design variables. However, it may be difficult to determine an appropriate finite step size for each design variable. The adjoint approach has been shown to be efficient if the number of responses is smaller than the number of design variables [18].

The coupled adjoint method for aerostructural sensitivities has been introduced by [14]. Since then, the coupled adjoint approach has been applied to multiple high-fidelity aerostructural optimization [5, 7, 11, 19–22]. However, the number of structural responses is usually larger than the number of structural design variables. Thus, the structural responses like stress, strain, or structural stability can be aggregated for example by utilizing Kreisselmeier-Steinhauser (KS) functions [7, 11, 19, 22–24]. This approach reduces the number of constraints, but it yields conservative designs.

Another approach is followed by a recent aerostructural optimization study at DLR, where the aerodynamic shape design variables are optimized at a top level using high-fidelity RANS computation and a structural design and optimization process on a sublevel [9]. This approach guarantees a feasible structural design at each optimization step. It also takes advantage of the maturity of structure optimization methods, where the number of design variables and the number of constraints can be fairly larger than for aerodynamic optimization. The CRM has been used to demonstrate the capabilities of the process by maximizing lift over drag. Since the sensitivities of the structural responses like mass with respect to aerodynamic design variables are not available in the process, no multidisciplinary objectives or constraints can be formulated.

Thus, this study continues the work of [9] and integrates the structural responses and sensitivities. The structural design process is treated as a black box to compute sensitivities with FD. Although the FD method is costly for many design variables, it is believed that the number of interesting shape variables is limited. While the structural design routine is running, only a small portion of the available CPU's is used. Hence running the FD scheme in parallel does not yield additional costs. Since the structural design process is not sensitive to all aerodynamic design variables [25], only selected parameters of a function representing the wing's twist over the wing's span are chosen as design variables.

2 PROCESS DESCRIPTION

2.1 STRUCTURAL DESIGN USING MONA

The structural design process at the DLR Institute of Aeroelasticity, referred to as MoNa, combines the in-house developed model generator ModGen and the commercial software MSC Nastran. An overview of the process flow is provided by Figure 1. ModGen is used to generate the following models for complete aircraft configurations: structural finite-element model, aerodynamic vortex lattice model, aerostructural coupling model, mass model, and structural optimization model. Additionally, ModGen includes a preliminary cross-sectional sizing of wing structures. Initial estimated loads are used to determine cross-sectional properties of the primary wing box structure. Those properties are wall thicknesses for skins, spars and ribs or stiffener and stringer dimensions. Semi-empirical equations from light weight design are used to compute allowable stress values, considering material strength, fatigue and structural stability (buckling). The structural variables are then adjusted to stay below the allowable stress limits for a set of dimensioning loads. Further information can be found in [26]. The preliminary design and the loads computation are performed in an iterative loop, referred to as *presizing loop* in Figure 1. Usually convergence of the cut load distribution is reached after five executions. The relative change of the root bending moment between the last iterations is $0.2\,\%$.

However, changing the structural design variables affects the mass distribution of the wing, leading to different values for the total mass and the center of gravity. To ensure comparable structural models for the loads analysis, a compensation mass is added to the load reference axis of the fuselage. It is adjusted after each design step to ensure that the center of gravity of the corresponding mass configuration of the aircraft does not change.

Once the presizing loop is converged, the *optimization loop* is executed. The wall thicknesses for skins, spars and ribs of the primary wing box are optimized by minimizing the struc-

tural mass. The constraints for the structural optimization are minimum wall thickness, maximum allowable stress and buckling failure index for each shell element. To ensure consistency, loads are computed again using the updated stiffness and mass model. After three to five iterations of the optimization loop, the structural design does not change considerably and the structural mass changes by 0.01 %.

Table 1: Flight states for the 2.5G Pull-Up at MTOW 260t.

ID	H in m	V_{EAS} in kn	Ma	$\bar{q}$ in Pa	PITCH
1	0	374	0.57	22794.9	0.001385
2	0	430	0.65	30111.3	0.001048
3	7459	374	0.92	22794.9	0.000632
4	6523	430	0.99	30111.3	0.000532

For demonstration purposes four 2.5g pull-up maneuver are used as design load cases, which are listed in Table 1.

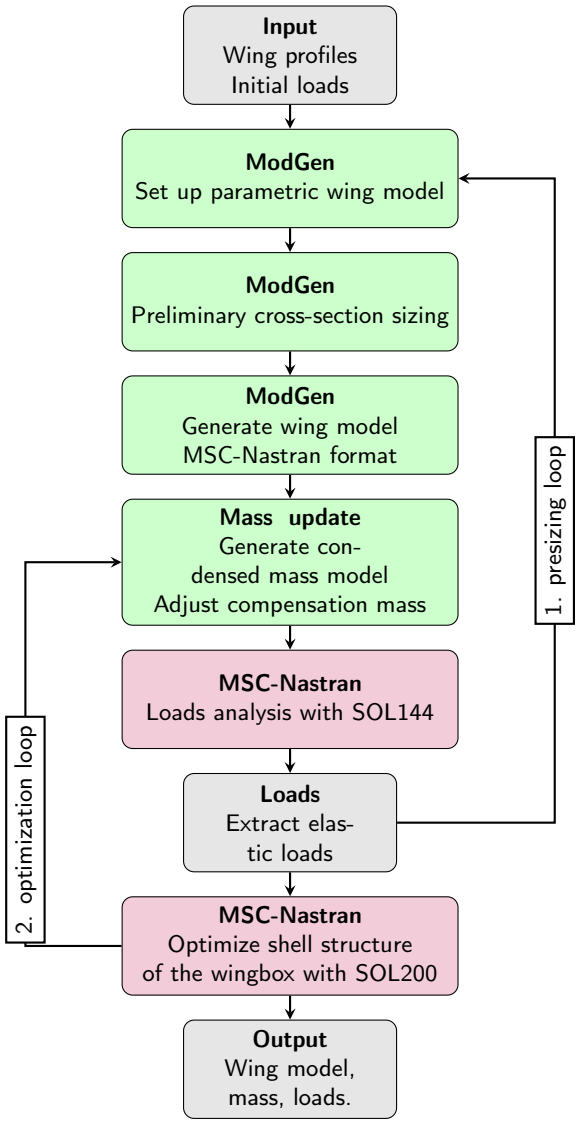

Figure 1: Process flow of MoNa.

2.2 AEROELASTIC PERFORMANCE ANALYSIS

The aeroelastic performance analysis evaluates the aerodynamic coefficients for the elastic aircraft at a single operational point. The DLR's Reynolds-averaged Navier-Stokes flow solver TAU is used [27]. Typically, the design cruise Mach number and altitude are taken as well as a medium fuel mass configuration (e.g. 50 %). A target lift coefficient of C_L is achieved by altering the angle of attack every 50th iteration step. The update from jig-shape to flight shape and the elevator deflection to satisfy the trimming condition $C_{my} = 0$ is achieved by mesh deformation. In an interval of 500 iterations the elastic wing deflection is computed and a new elevator deflection angle is determined. Then, the CFD grid is deformed accordingly using radial basis functions. After 2500 iterations, the flight shape is assumed to be reached and no further mesh deformation is executed. In total, 5000 iterations including seven mesh-updates show adequate convergence of the density residual ($|\Delta\rho| < 10^{-5}$). The order of execution of the different modules is layed out in Figure 2.

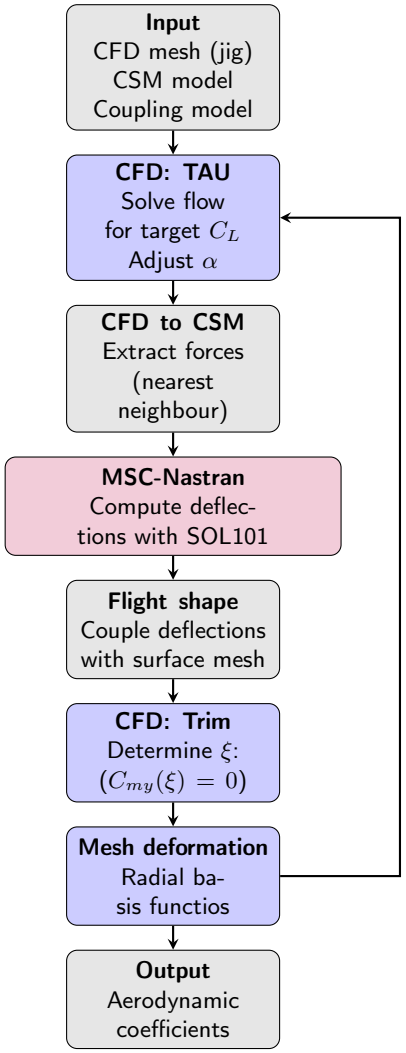

Figure 2: Process flow of the hifi performance analysis.

2.3 GRADIENT COMPUTATION

The gradients of aerodynamic responses f_a with respect to the design variables $\boldsymbol{x}_a$ need to be corrected by the stability coefficients to account for the trimming condition. A similar

approach to [20, 28] is followed.

$$C_L = 0.536 \qquad C_{my} = 0 \tag{1}$$

For stationary horizontal flight, the trimming variables are the angle of attack $\alpha(\boldsymbol{x}_a)$ and the elevator deflection $\xi(\boldsymbol{x})$. The trimming variables are dependent on the design variables, as they change the stability derivatives by altering the force and moment distribution. Therefore, the derivative of an aerodynamic cost function $f_a(\boldsymbol{x}_a, \alpha(\boldsymbol{x}_a), \xi(\boldsymbol{x}_a))$ for the trimmed flight is written as

$$\frac{df_s}{dx_{a,i}} = \frac{\partial f}{\partial x_{a,i}} + \frac{\partial f}{\partial \alpha}\frac{\partial \alpha}{\partial x_{a,i}} + \frac{\partial f}{\partial \xi}\frac{\partial \xi}{\partial x_{a,i}}. \tag{2}$$

The partial derivatives of the trim variables with respect to the design variables are determined by approximately satisfying the trim condition. Since the target lift coefficient and the pitching moment are kept constant, they are not variables. Therefore, their derivatives need to be zero which yields:

$$0 = \frac{\partial C_L}{\partial x_{a,i}} + \frac{\partial C_L}{\partial \alpha}\frac{\partial \alpha}{\partial x_{a,i}} + \frac{\partial C_L}{\partial \xi}\frac{\partial \xi}{\partial x_{a,i}} \tag{3}$$

$$0 = \frac{\partial C_{my}}{\partial x_{a,i}} + \frac{\partial C_{my}}{\partial \alpha}\frac{\partial \alpha}{\partial x_{a,i}} + \frac{\partial C_{my}}{\partial \xi}\frac{\partial \xi}{\partial x_{a,i}} \tag{4}$$

The sensitivities $\frac{\partial \alpha}{\partial x_{a,i}}$ and $\frac{\partial \xi}{\partial x_{a,i}}$ are then determined by rearranging Equations 3 and 4.

$$\frac{\partial \xi}{\partial x_{a,i}} = \frac{\frac{\partial C_{my}}{\partial \alpha}\frac{\frac{\partial C_L}{\partial x_{a,i}}}{\frac{\partial C_L}{\partial \alpha}} - \frac{\partial C_{my}}{\partial x_{a,i}}}{\frac{\partial C_{my}}{\partial \xi} - \frac{\partial C_{my}}{\partial \alpha}\frac{\frac{\partial C_L}{\partial \xi}}{\frac{\partial C_L}{\partial \alpha}}} \tag{5}$$

$$\frac{\partial \alpha}{\partial x_{a,i}} = \frac{-1}{\frac{\partial C_L}{\partial \alpha}}\left(\frac{\partial C_L}{\partial x_{a,i}} + \frac{\partial C_L}{\partial \xi}\frac{\partial \xi}{\partial x_{a,i}}\right) \tag{6}$$

The aerodynamic sensitivities like $\frac{\partial f_a}{\partial x_{a,i}}$ or $\frac{\partial C_l}{\partial x_{a,i}}$ are determined by using the adjoint approach.
Structural response sensitivities with respect to aerodynamic shape changes are computed by using the FD approach (Equation 7).

$$\frac{df_s}{dx_{a,i}} = \frac{f_s(x_{a,i} + \Delta x_{a,i}) - f_s(x_{a_i})}{\Delta x_{a,i}} + \mathcal{O}(\Delta x_{a,i}) \tag{7}$$

The MoNa process is called as a black box and the sensitivities are computed by altering the design about a finite step $\Delta x_{a,i}$. Since this derivative is a linear approximation, the error grows with the step size. In case the step size is too small, numerical noise, process noise and modelling errors lead to unreasonable or imprecise derivatives.

2.4 OPTIMIZATION PROCESS

The optimization process is controled by the framework PyRanha, developed at the Institute of Aerodynamics and Flow Technology (DLR). It provides several gradient-free and gradient-based optimization algorithms to solve unconstrained and constrained optimization problems. In case no constraints are formulated a Variable Metric Method (VMM) is used and otherwise the Sequential Quadratic Programming (SQP) is chosen to solve the optimization task. The execution of the different process modules is presented in Figure 3.

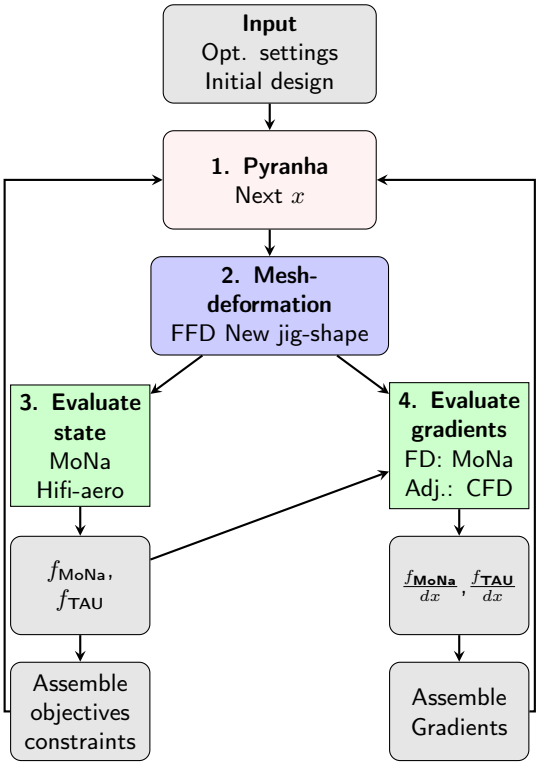

Figure 3: Process flow of the aerostructural optimization.

3 SIMULATION MODELS

3.1 NASA COMMON RESEARCH MODEL

The CRM has been developed to provide a full transport aircraft geometry including experimental data. The basic geometric characteristics are shown in Table 2. The original CRM is described in [29] and multiple experimental studies can be found in [30–33]. Comparisons between aerodynamic simulations and the experimental data are provided for example by [34–36]. Multiple aerodynamic optimization studies of the CRM and the CRM wing are conducted as well with different levels of fidelity [37–39]. Since the CRM geometry is in the $1g$ flight shape, multiple jig-shapes of the wing are provided by [8, 13, 16]. Aerostructural optimization studies for different configurations of the CRM are conducted as well [5, 8, 9, 16, 40, 41].

Table 2: CRM characteristics according to [29].

Property	symbol	value
Mean aerodynamic chord	C_{MAC}	7 m
Wing area	S_{ref}	387.7 m^2
Wing span	b	58.76 m
Wing sweep (25 %)	Λ_{25}	35°

3.2 GLOBAL FE MODEL

The global FE model of the whole aircraft is generated by ModGen, depicted in Figure 4. All components are made of aluminium. The Young's modulus is set to 74 GPa, the shear modulus to 28.5 GPa and the density is assumed to be 2800 kg m^{-3}

Skins, spars and ribs are represented by shell elements and the fuselage, the engine's pylon, stringers, stiffeners, and spar-caps are modeled by beam elements. The engine itself is modeled as a point mass. The connection between pylon and engine as well as between pylon and wing is realized by beam elements. A breakdown of the number of elements for each component is provided in Table 3.

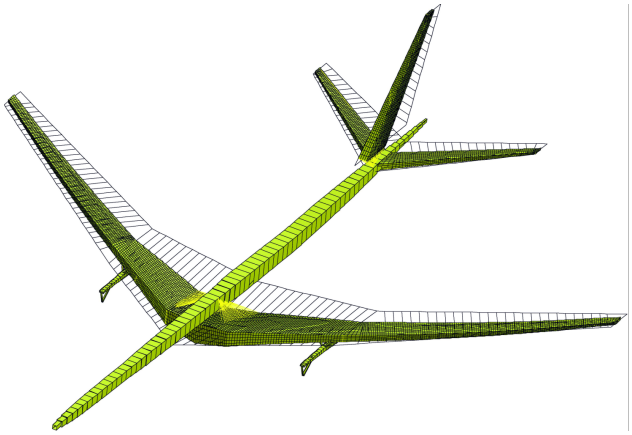

Figure 4: FEM model

Table 3: Number of elements.

Component	Shell	Beam
Fuselage	0	77
Wing	2×8669	2×12443
Pylon	0	2×16
HTP	2×2185	2×2899
VTP	3104	4259
Total	24812	35052

The mass model of the whole aircraft consists of concentrated masses, which are distributed along the load reference axis (LRA, Figure 8). An example is shown in Figure 5. The mass and moment of inertia properties are merged from the primary structure, secondary structure, systems, fuel, payload and passengers.

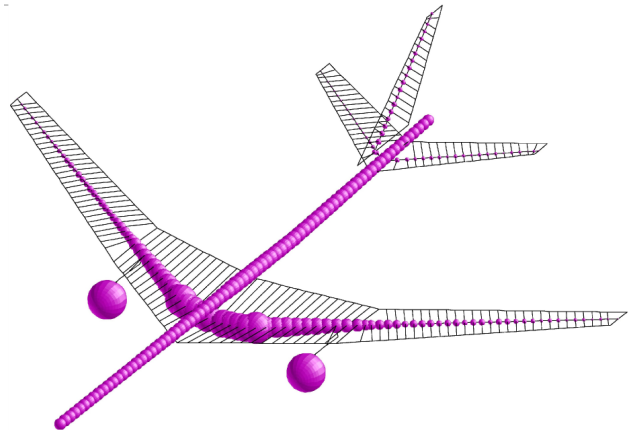

Figure 5: Condensed mass model

3.3 AERODYNAMIC MODELS

As the loads analyis usually needs to consider a large amount of different load cases, the fast but subsonic vortex lattice method is used for static load cases. The panel model is shown in Figure 6 and the discretization is provided by Table 4. The fuselage is prepresented by a panel discretization of the internal wing area.

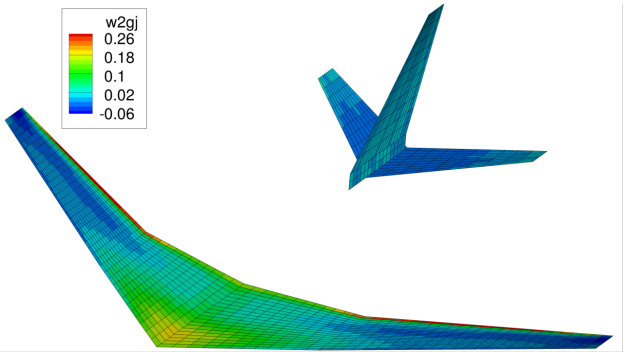

Figure 6: Aerodynamic Vortex Lattice model including correction factors (w2gj) for the panel normal vectors to account for twist and camber.

Table 4: Number of aerodynamic panels.

Component	$n_{\text{span}} n_{\text{chord}}$	Total
Wimpress	$2 \times 3 \times 20$	120
Wing	$2 \times 37 \times 20$	1480
HTP	$2 \times 10 \times 10$	200
VTP	12×15	180
VTP rudder	10×5	50
Total		2030

Twist and camber information of the lifting surfaces are taken from the parameterized geometry model of the wing and used to correct the normal vector of each panel (MSC Nastran W2GJ matrix).

The high-fidelity aerodynamic performance evaluation is achieved by solving the RANS equations at cruise flight. The turbulence model is a one equation Spalart-Allmaras model. The CFD grid is a slightly modified version of the grid, used previously in the aerostructural optimization study of Keye et. al [9]. The grid consists of 7 million nodes, and 200,000 surface nodes. In the vicinity of the solid walls, the viscous boundary layer is discretized by 43 cells normal to the wall. The distance between the aircraft and the far field boundaries is approximately 50 times the wing's span.

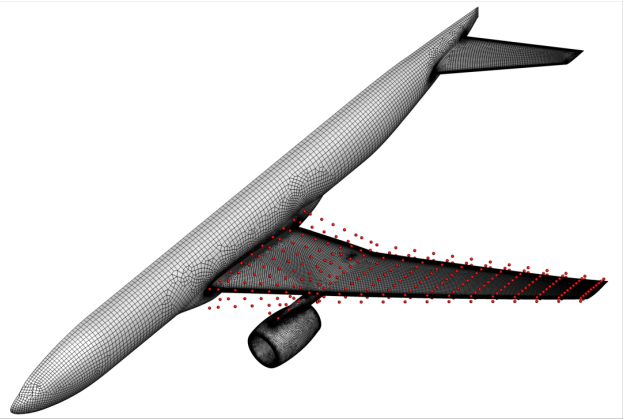

Figure 7: Surface discretization of the CRM and control-points (red) of the FFD-box.

3.4 AEROSTRUCTURAL COUPLING MODELS

Static aeroelastic analysis requires a coupling scheme between the two disciplines to enable the force/displacement transfer. For the loads analysis, the disciplines are coupled monolithically. The aerodynamic panels in Figure 6 are coupled with the stiffness model in Figure 4 via the load reference axis, shown in Figure 8. Aerodynamic forces are splined to the nodes of the load reference axis and nodes at the wing's and tail's leading and trailing edges. Those nodes (green) are linked rigidly to the load reference axis as well. The nodes of the LRA are positioned approximately at the center of ribs. From there, the forces are distributed to the nodes at the rib's outer edges.

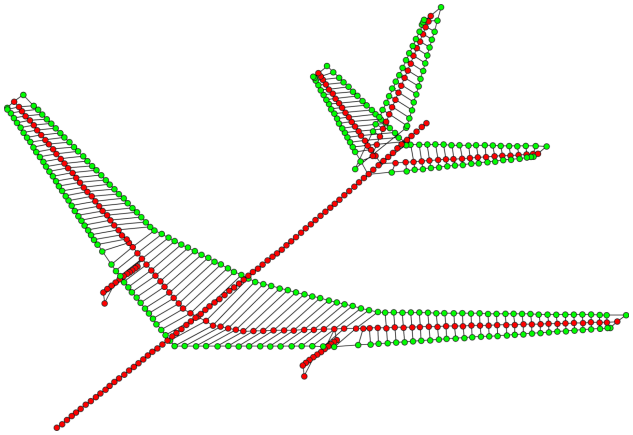

Figure 8: Nodes on the load reference axis in red. Grids of leading and trailing edges in green

A different coupling model is used for the high-fidelity performance analysis. The aerodynamic forces are integrated at the coupling nodes, which are shown in Figures 9 and 10. Those coupling nodes are generated by slicing the jig-shape surface-mesh of the wing at the nodes of the LRA for each design step. The slicing planes are oriented orthogonal to the load reference axis.

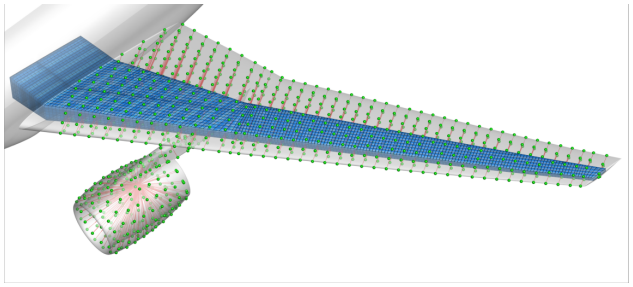

Figure 9: Integration points (green) and the rigid interface to the LRA (red) to couple the CFD-surface with the structure (blue).

Once the nodes are determined, the forces are rigidly transferred to the corresponding node on the LRA. The linear static solver of MSC Nastran is used to compute the deflections of the wing. The displacements of a set of the coupling nodes build the base for the mesh deformation using radial basis functions.

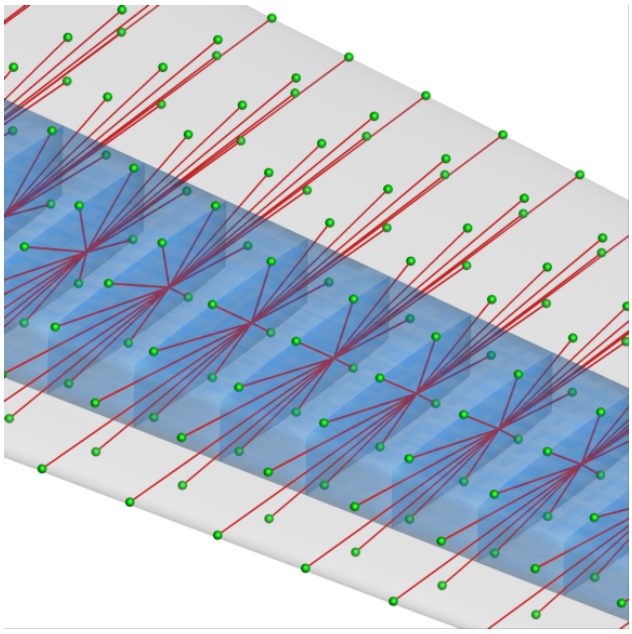

Figure 10: Integration points (green) and the rigid interface to the LRA (red) to couple the CFD-surface with the structure (blue).

3.5 OPTIMIZATION MODELS

3.5.1 WING STRUCTURE

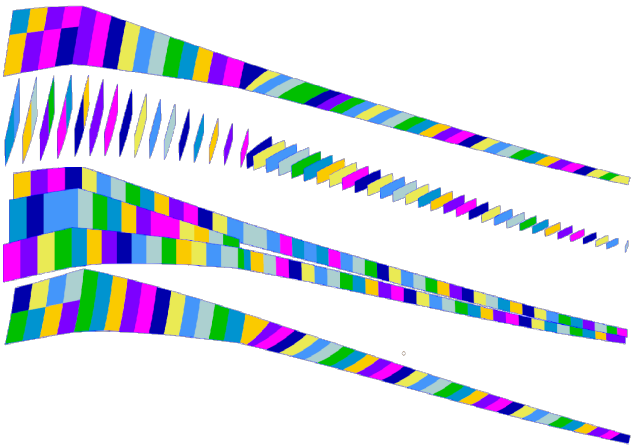

Figure 11: Design fields for the structural optimization process.

Table 5: Distribution of the 259 design fields per component.

Component	region	No. design fields
Skins		**100**
	Upper, CWB	8
	Lower, CWB	8
	Upper, inboard, outboard	42
	Lower, inboard, outboard	42
Ribs		**52**
	CWB	10
	inboard, outboard	42
Spars		**107**

As in [9], the wall thicknesses of the wing box are optimized for minimum weight. The structure is decomposed into design fields which are framed by ribs and spars, as depicted in Figure 11. In total 259 design fields are used (See Table 5). The objective is to minimize the structural mass by satisfying 17334 maximum stress constraints and 8667 buckling constraints.

3.5.2 AERODYNAMIC SHAPE PARAMETERIZATION

The design of the aerodynamic jig-shape is achieved by the Free-Form Deformation (FFD) technique [42]. This method requires a control box, which consists of control points, shown as red nodes in Figure 7. Displacements of the control points are used to deform the internal object via trivariate Bernstein polynomials. A major benefit is that design changes are smooth and the same mesh can be used. Thus this proces does not need a CAD tool or an automatic mesh generation tool.
The used FFD-box consists of 21 spanwise sections with each 10 nodes on the top and on the bottom, summing up to 420 nodes.

4 OPTIMIZATION OF THE WING TWIST

4.1 FLIGHT CONDITION

The aerodynamic performance analysis is evaluated at a cruise flight speed of $Ma = 0.85$, a Reynolds number of $Re = 46.40 \times 10^6$, and an altitude of 10 668 m. The target lift coefficient is $C_L = 0.536$.

4.2 TWIST PARAMETERIZATION

The aerodynamic shape parameterization alters the FFD control points. However it was observed by [9], that the selected aerodynamic shape changes hardly affected the structural responses. Displacing each node separately results in a large design space and the structural responses may be hardly sensitive to those changes [25]. Therefore, the wing's twist is chosen as design parameter, as it affects both disciplines and causes larger design changes.

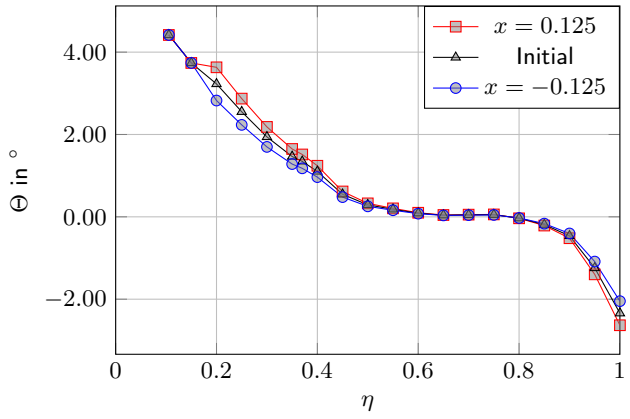

Figure 12: Limits of the scaled twist parameterization.

Two different twist parameterizations were developed and implemented. The first scales the entire twist distribution by a scaling factor x.

$$\Theta(\eta) = (1 + x)\Theta^{\text{initial}}(\eta) \tag{8}$$

A positive scaling factor increases the twist at the inboard section and reduces it at the outboard section, as the distribution shows a zero-crossing. Thus, a positive value shifts the load distribution inboard, reducing the root-bending-moment. Since the lift distribution deviates further from the elliptic shape, a drag increase is expected. As the initial twist distribution is only scaled, the zero-crossing of the CRM's twist remains at the same spanwise location. Only one design parameter is used.

However, the ranges of design parameters are limited, because they deform the surface mesh which can lead to mesh distortion. A flawed mesh would require a new mesh and an automated mesh generation process, which is not part of the process. Critical locations for mesh deformation are at the intersection of the fuselage and the trailing edge and at the exhaust of the nacelle. As changing the twist at the wing's root is likely to cause negative cells, this parameter is excluded from the optimization. Freezing the mounting angle of the wing means that a compromise between optimal fuselage inclination and optimal twist distribution cannot be found. Scaling the rest of the twist distribution was successfully tested for $\pm 12.5\,\%$. The limits of the design space are visualized in Figure 12.

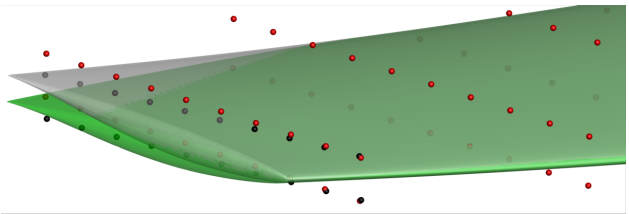

Figure 13: Rigid rotation of FFD control points about the leading edge causing a 5° variation of the tip twist.

The second parameterization adds an offset to each section, totalling in a maximum of 21 design parameter. An example of the second parameterization method is shown in Figure 13. The red nodes are the initial FFD control points and the black are displaced by a rigid rotation about the leading edge.

For the section-wise twist parameterization, larger variations of $\pm 5°$ are possible. This becomes even more robust, when the inboard sections are excluded from the design parameters.

4.3 FINITE STEP SIZE INVESTIGATION

As the structural sensitivities are determined by using FD, a reasonable step size needs to be estimated.

The first parameterization needs only one scaling parameter. The derivative of the bending moment over the wing's span with respect to different finite steps of the scaling factor Δx is shown in Figure 14. An examination of the curves indicates that all finite steps seem to cause a similar gradient distribution. Hence, the finite step could be any of the investigated values. This means that even scaling the twist by 0.5 % causes a significant change of the bending moment.

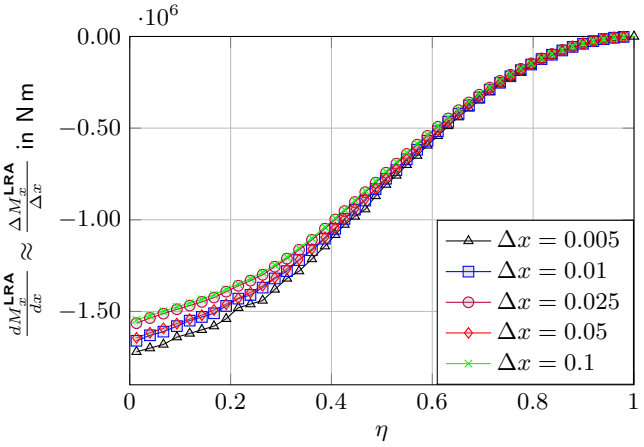

Figure 14: Stepsize investigation for the scaled twist parameterization.

However, the sensitivities are derived by applying MoNa as a blackbox, where the structural optimization loop is neglected. The reason for neglecting the structural optimization loop was that the nonlinear suboptimization caused imprecise gradients for small step sizes. This is demonstrated in Figures 15 and 16 where the twist is only varied at section 10 ($\eta = 0.5$). The root bending moment sensitivity for the MoNa process with the optimization loop has a negative sign for small step sizes and a positive sign for larger step sizes. Without the optimization loop, the gradient seems to be almost independent of the step size. Note, the sensitivities reach the same level for larger step sizes $\Delta\Theta > 1$. The mass sensitivity with respect to twist variations at section 10 (Figure 16) changes the sign if the structural optimization loop is excluded. Without the optimization loop, all mass changes are positive with respect to a positive change of the twist. This is in good agreement with the increase of the root bending moment. However, including the structural suboptimization shows the exact opposite. Even though the root bending moment increases, the structural mass decreases.
The step size investigation shows that the MoNa process is not suitable for fine variations of the twist parameterization if the structural optimization is used. Therefore, the structural optimization is excluded from the MoNa process and only the preliminary cross-section sizing is included.

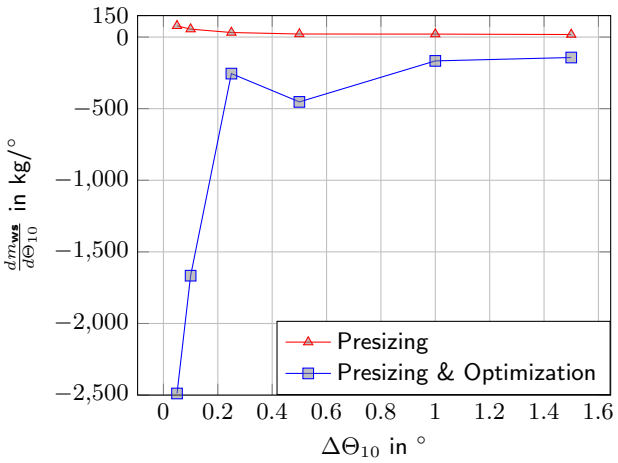

Figure 15: Gradient of the wing's structural mass versus finite step size. Stepsize investigation for profile section 10 ($\eta = 0.5$).

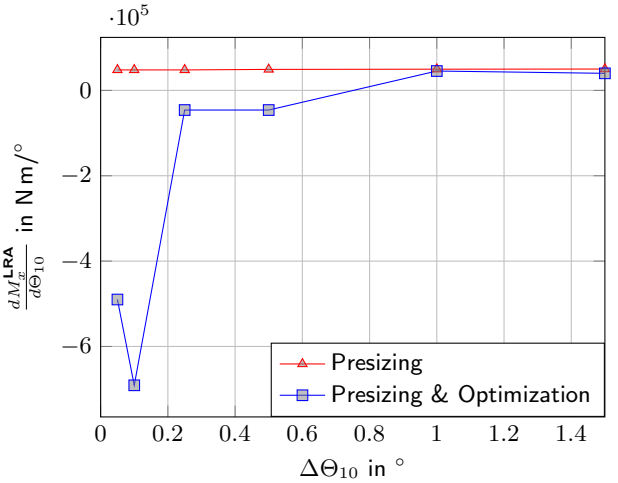

Figure 16: Gradient of the root bending moment versus finite step size. Stepsize investigation for profile section 10 ($\eta = 0.5$).

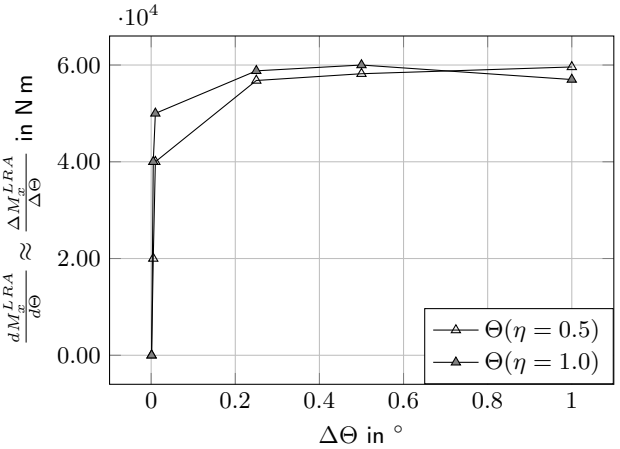

Figure 17: Stepsize investigation for the sectionwise twist parameterization using the MoNa process as blackbox without the structural optimization.

The sensitivities of the root bending moment with respect to separate variations of the twist at sections $\eta = 0.5$ and $\eta = 1.0$ is shown in Figure 17. Therein, it is visible that fine variations of $\Delta\Theta_i = 0.005°$ already allow accurate sensitivities.

4.4 OPTIMIZATION OF THE SCALED TWIST DISTRIBUTION

The scaling factor is used as design parameter for the first optimization test. A mixed objective is formulated by multiplying the maximum root bending moment ($M_x^{\mathsf{LRA}}(\eta = 0.1)$) from the loads analysis by the drag coefficient from the aerodynamic performance analysis. As no constraints are formulated, the VMM is used to solve the optimization task.

The development of the objective is shown in Figure 18. Apparently, the objective is linearly dependent on the design variable. Hence, the optimizer ends up in an optimum at the limit of the scaling parameter of $x = 0.125$.

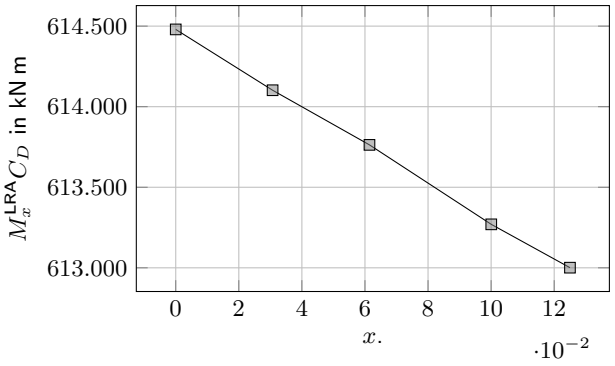

Figure 18: Development of the objective $M_x^{\mathsf{LRA}} \times C_D$ for different designs.

The disciplinary responses (M_x^{LRA} from MoNa and C_D from TAU) are shown in Figure 19. Both responses are linearly dependent on the scaling parameter. Also, their trends are opposite to each other, as it is expected due to the shift of the lift distribution further inboard. Although the aerodynamic performance is reduced, the composed objective in Figure 18 is hardly affected.
The root bending moment is reduced by 226.4 kN m which is $-1.05\,\%$ of the initial value. Consequently, the right wingbox becomes 141 kg ($-1.17\,\%$) lighter. However, the lift over drag ratio worsens by 0.152 ($-0.81\,\%$).

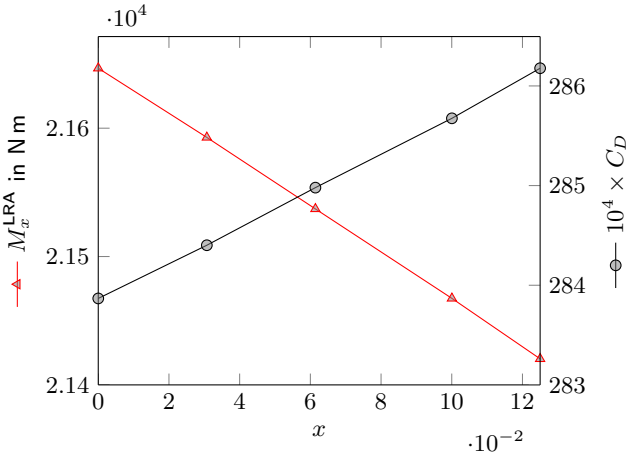

Figure 19: Development of M_x^{LRA} and C_D for different design cycles.

4.5 OPTIMIZATION OF THE OUTBOARD TWIST DISTRIBUTION

The outboard twist distribution is optimized at 12 sections between $\eta = 0.45$ and $\eta = 1$. The twist variation at each section is limited by $x \in [-4°, \ldots, 2°]$. Mesh deformation due to those shape changes did not cause distorted cells.

4.5.1 FIRST OBJECTIVE FUNCTION

Again, the composed objective $M_x^{\mathsf{LRA}} \times C_D$ is minimized using the VMM. The development of the responses for the different design steps is shown in Figure 20. The values are normalized by the responses for the initial design. An optimum is found at design cycle 8. For this design, the bending moment is 2591.2 kN m ($-11.94\,\%$) smaller, causing a 1481 kg ($-12.22\,\%$) lighter right wing box. However, the opposite development of the drag coefficient in Figure 20 already indicates a severe degradation of the aerodynamic performance. The lift over drag ratio drops by 1.57 ($-8.31\,\%$) from 18.86 to 17.30.

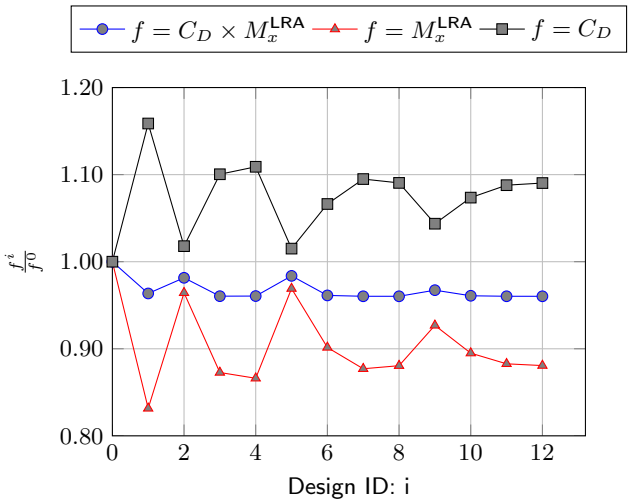

Figure 20: Development of the responses for each design cycle.

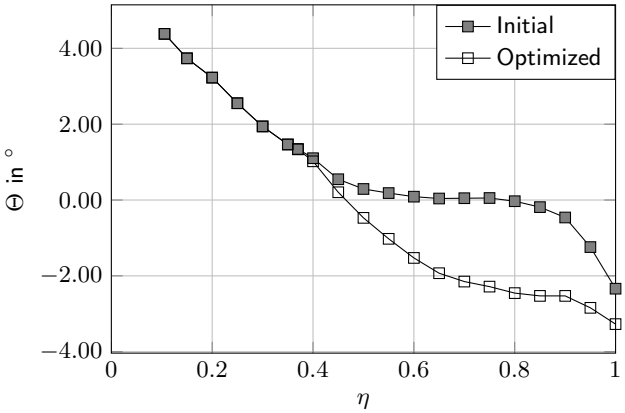

Figure 21: Initial and final twist distribution.

The optimized twist distribution deviates strongly from the initial distribution (Figure 21). Instead of the *cubic* shape of the CRM's twist distribution, the twist becomes almost linear. As all twist angles of the outboard sections are negative for the optimum design, the lift is shifted further inboard (Figure 22). Thus the outboard section of the wing is unloaded.

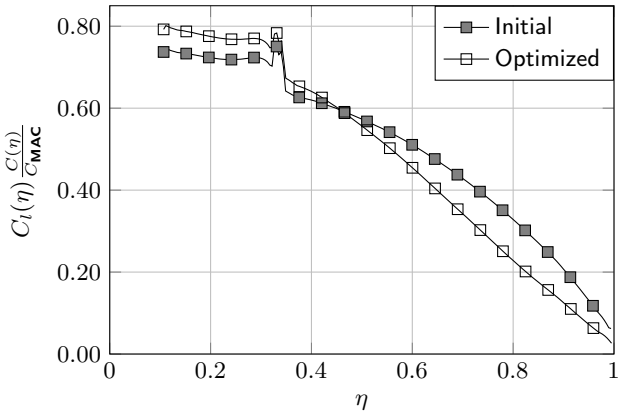

Figure 22: Initial and final lift distribution.

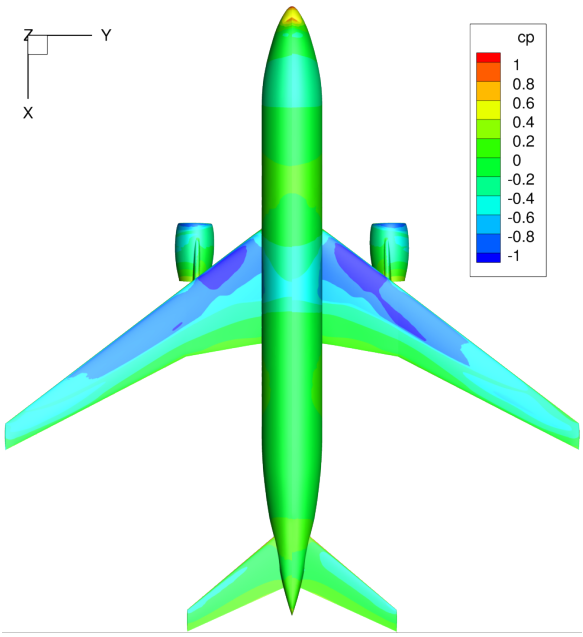

Figure 23: Initial (left) and optimized (right) pressure distribution for the outboard twist optimization minimizing $M_x^{\mathsf{LRA}} \times C_D$.

Figure 23 shows the pressure distribution for the baseline and the optimized twist. It is evident that the inboard sections are loaded and the outboard sections unloaded, leading to the lift distribution shown in Figure 22.

4.5.2 SECOND OBJECTIVE FUNCTION

A last optimization task is formulated by maximizing the range of the CRM based on the Breguet formula. Note, since the lift coefficient does not change within the process, it is a constant in the range equation.

$$R(C_D, m_{\mathsf{TO}}) = \frac{C_L}{C_D} \ln\left(\frac{m_{\mathsf{TO}}}{m_{\mathsf{TO}} - m_{\mathsf{F}}}\right) \tag{9}$$

$$\frac{dR}{dx_i} = -\frac{C_L}{C_D^2} \ln\left(\frac{m_{\mathsf{TO}}}{m_{\mathsf{TO}} - m_{\mathsf{F}}}\right) \frac{dC_D}{dx_i} + \frac{C_L}{C_D} \frac{m_{\mathsf{F}}}{m_{\mathsf{TO}} m_{\mathsf{F}} - m_{\mathsf{TO}}^2} \frac{dm_{\mathsf{TO}}}{dx_i} \tag{10}$$

The take off mass is composed of

$$m_{\mathsf{TO}} = 164\,000\,\mathrm{kg} + 2m_{\mathsf{WS}} + m_{\mathsf{F}} \tag{11}$$

where the fuel mass is $m_{\mathsf{F}} = 72\,000$ kg.

The range factor R is shown in Figure 24 for the 20 design iterations. The optimum is design 20, which shows an improvement from $R = 6.47$ to $R = 6.51$, which is a $+0.6\%$ increase in range.

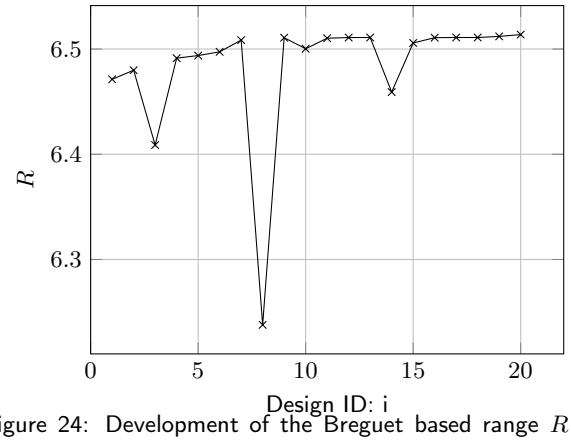

Figure 24: Development of the Breguet based range R for each design step.

The two variables in the optimization process are the wing's structural mass and the aerodynamic performance, shown for the designs in Figure 25. The aerodynamic performance increases from $C_L/C_D = 18.88$ to $C_L/C_D = 19.03$ ($+0.7\%$ increase). However, the right wingbox becomes heavier from $m_{\mathsf{WS}} = 12\,158$ kg to $m_{\mathsf{WS}} = 12\,409$ kg ($+2\%$).

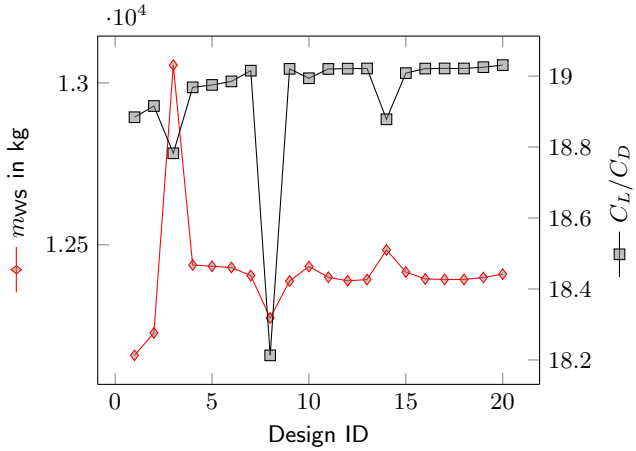

Figure 25: Development of the wing's structural mass and the aerodynamic performance.

Apparently, the aerodynamic performance in Figure 25 and the range factor in Figure 24 show very similar developments. Investigating equation 9, it is evident, that the aerodynamic performance is much more dominant in this composite function. The small changes of 502 kg (Complete wingbox) relative to the landing mass of approximately 184 000 kg do not have a considerable impact on the range estimate.

The increased aerodynamic performance can be explained by looking at the optimized twist distribution in Figure 26 and the lift distribution in Figure 27. Between $\eta = 0.6$ and $\eta = 0.95$, the twist is increased, which leads to a more elliptical shape of the lift distribution. Although not all drag components are decomposed, this could indicate a reduction of the induced drag. The pressure distribution in Figure 28 also confirms the outboard loading of the wing.

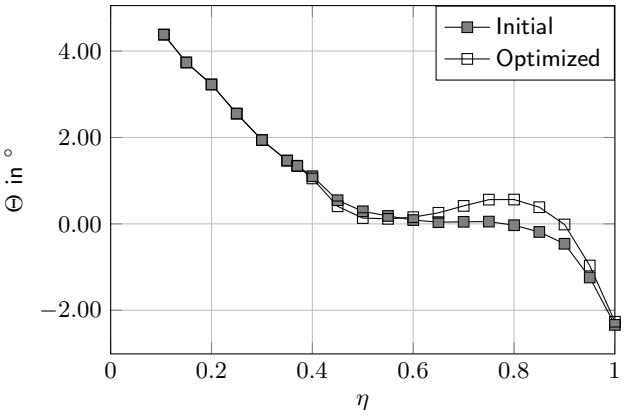

Figure 26: Initial and optimized twist distribution for the Breguet based range optimization.

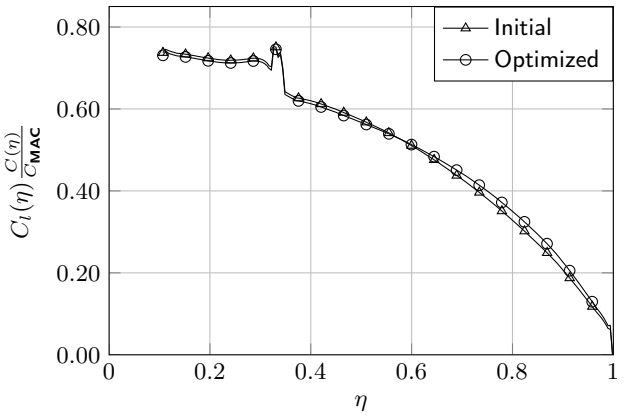

Figure 27: Initial and optimized lift distribution for the Breguet based range optimization.

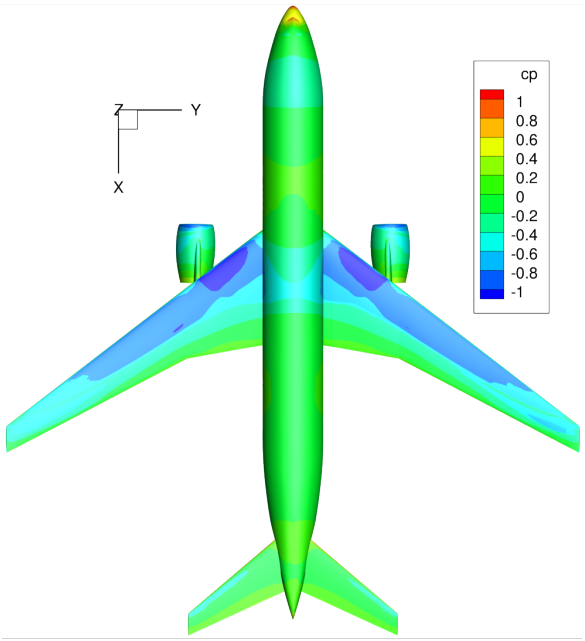

Figure 28: Initial (left) and optimized (right) pressure distribution for the outboard twist optimization maximizing R.

5 CONCLUSION AND OUTLOOK

A high fidelity aerostructural optimization of the wing's twist is performed. The structural subprocess MoNa is now integrated at the top level of the optimizer, which allows multidisciplinary response formulations for coupled aero-structural optimization tasks. However, the complete nonlinear structural suboptimization process in MoNa does not show to be sensitive enough for small design changes. Finite steps were too large, relative to the considered box limits of the design parameters. Therefore, the structural optimization loop is neglected and only preliminary cross-sectional sizing of the wingbox structure is used.

Two different parameterizations of the wing's twist were developed and applied as design space. Negative cells at the fuselage/trailing-edge intersection and the engine's nacelle due to mesh deformation limited the design space. Therefore, the wing's twist could only be optimized at the outboard sections ($0.45 \leq \eta \leq 1$).

Also, two different multidisciplinary objectives have been defined for the optimization. The first is the product of the maximum root bending moment and the drag coefficient. The second bases on the Breguet range equation. In both cases, an imbalance between the disciplines was detected, which is caused by the objectives and the sensitivities.

Minimizing the product of maximum root bending moment and drag coefficient yields a design which strongly favors the structural discipline. It was observed, that the design sensitivites of the structural discipline were dominant.

The Breguet based range optimization increased the range by improving the aerodynamic performance. However, the Breguet based formulation is strongly in favor of the aerodynamic discipline. Hence, the increased structural mass does not provide a large enough impact on the range.

For future studies it is aimed to investigate multiple objective functions, which are more relevant to aircraft industries (e.g. cost, fuel burn). The imbalance between the disciplines may also be reduced by imposing disciplinary and multidisciplinary constraints. For example flutter constraints, aileron reversal and longitudinal static stability could be accounted for.

For the structural part, more load cases are needed and the subsonic VLM aerodynamics has to be improved. Since high-fidelity aerodynamic simulation models and data are already available in the process, CFD based correction methods for VLM should be integrated. Also a change of material from aluminum to composites should be made to apply aeroelastic tailoring methods.

Another challenge is to incorporate mesh deformation techniques which can deal with large shape variations. It is necessary to include inboard sections of the wing in the design space to uncover actual potential in high-fidelity MDO.

REFERENCES

[1] Papageorgiou, A.; Tarkian, M.; Amadori, K.; Ölvander, J.: *Multidisciplinary Design Optimization of Aerial Vehicles: A Review of Recent Advancements*: International Journal of Aerospace Engineering, Hindawi Limited, P.: 1–21, May 2018.

[2] Schuhmacher, G.; Murra, I.; Wang, L.; Laxander, A.; O'Leary, O.; Herold, M.: *Multidisciplinary Design Optimization of a Regional Aircraft Wing Box*. In: *9th AIAA/ISSMO Symposium on Multidisciplinary Analysis and Optimization*, American Institute of Aeronautics and Astronautics, Sept. 2002.

[3] Elham, A.; van Tooren, M. J. L.: *Multi-fidelity wing aerostructural optimization using a trust region filter-SQP algorithm*: Structural and Multidisciplinary Optimization Nr. 5, P.: 1773–1786, May 2017.

[4] Martins, J. R. R. A.: *A Coupled-Adjoint Method For High-Fidelity Aero-Structural Optimization*. Phd-Thesis. Department of Aeronautics and Astronautics, Stanford University, Oct. 2002.

[5] Kenway, G. K.; Martins, J. R. R. A.: *Multipoint High-fidelity Aerostructural Optimization of a Transport Aircraft Configuration*: Journal of Aircraft Nr. 1, American Institute of Aeronautics and Astronautics (AIAA), P.: 144–160, Jan. 2014.

[6] Oyama, A.: *Multidisciplinary Optimization Of Transonic Wing Design Based On Evolutionary Algorithms Coupled With Cfd Solver*. In: *SOLVER, Proceedings of European Congress on Computational Methods in Applied Sciences and Engineering*, 2000.

[7] Ghazlane, I.; Carrier, G.; Dumont, A.: *Aerostructural Adjoint Method for Flexible Wing Optimization*, 2012.

[8] Kenway, G.; Kennedy, G.; Martins, J. R. R. A.: *Aerostructural optimization of the Common Research Model configuration*. In: *15th AIAA/ISSMO Multidisciplinary Analysis and Optimization Conference*, American Institute of Aeronautics and Astronautics, June 2014.

[9] Keye, S.; Klimmek, T.; Abu-Zurayk, M.; Schulze, M.; Ilić, Č.: *Aero-Structural Optimization of the NASA Common Research Model*. In: *18th AIAA/ISSMO Multidisciplinary Analysis and Optimization Conference*, American Institute of Aeronautics and Astronautics, June 2017.

[10] Chittick, I. R.; Martins, J. R. R. A.: *An asymmetric suboptimization approach to aerostructural optimization*: Optimization and Engineering Nr. 1, Springer Nature, P.: 133–152, Apr. 2008.

[11] Martins, J. R. R. A.; Alonso, J. J.; Reuther, J. J.: *High-Fidelity Aero-Structural Design Optimization of a Supersonic Business Jet*. In: *Proceedings of the 43rd AIAA/ASME/ASCE/AHS/ASC Structures, Structural Dynamics, and Materials Conference*, 2002.

[12] Kenway, G. K. W.; Kennedy, G. J.; Martins, J. R. R. A.: *Scalable Parallel Approach for High-Fidelity Steady-State Aeroelastic Analysis and Adjoint Derivative Computations*: AIAA Journal Nr. 5, American Institute of Aeronautics and Astronautics (AIAA), P.: 935–951, May 2014.

[13] Klimmek, T.: *Parametric Set-Up of a Structural Model for FERMAT Configuration for Aeroelastic and Loads Analysis*: Journal of Aeroelasticity and Structural Dynamics Nr. 2, Department of Aerospace Engineering of Politecnico di Milano, P.: 31–49, May 2014.

[14] Reuther, J.; Alonso, J.; Martins, J. R. R. A.; Smith, S.: *A coupled aero-structural optimization method for complete aircraft configurations*. In: *37th Aerospace Sciences Meeting and Exhibit*, American Institute of Aeronautics and Astronautics, Jan. 1999.

[15] Piperni, P.; Abdo, M.; Fafyeke, F.: *The Application of Multi-Disciplinary Optimization Technologies to the Design of a Business Jet*. In: *10th AIAA/ISSMO Multidisciplinary Analysis and Optimization Conference*, American Institute of Aeronautics and Astronautics, Aug. 2004.

[16] Brooks, T. R.; Kennedy, G.; Martins, J. R. R. A.: *High-fidelity Multipoint Aerostructural Optimization of a High Aspect Ratio Tow-steered Composite Wing*. In: *58th AIAA/ASCE/AHS/ASC Structures, Structural Dynamics, and Materials Conference*, American Institute of Aeronautics and Astronautics, Jan. 2017.

[17] Goertz, S.; Ilić, Č.; Jepsen, J.; Leitner, M.; Schulze, M.; Schuster, A.; Scherer, J.; Becker, R.; Zur, S.; Petsch, M.: *Multi-Level MDO of a Long-Range Transport Aircraft Using a Distributed Analysis Framework*. In: *18th AIAA/ISSMO Multidisciplinary Analysis and Optimization Conference*, American Institute of Aeronautics and Astronautics, June 2017.

[18] Martins, J. R. R. A.; Hwang, J. T.: *Review and Unification of Methods for Computing Derivatives of Multidisciplinary Computational Models*: AIAA Nr. 11, American Institute of Aeronautics and Astronautics (AIAA), P.: 2582–2599, Nov. 2013.

[19] Chittick, I. R.; Martins, J. R. R. A.: *Aero-structural optimization using adjoint coupled post-optimality sensitivities*: Structural and Multidisciplinary Optimization Nr. 1, Springer Nature, P.: 59–70, Dec. 2007.

[20] Abu-Zurayk, M.; Brezillon, J.: *Shape Optimization Using the Aero-structural Coupled Adjoint Approach for Viscous Flows*. In: *Eurogen 2011*, 2011.

[21] Brezillon, J.; Ronzheimer, A.; Haar, D.; Abu-Zurayk, M.; Lummer, M.; Krüger, W.-R.; Natterer, F. J.: *Development and application of multi-disciplinary optimization capabilities based on high-fidelity methods*. In: *8th AIAA Multidisciplinary Design Optimization Specialist Conference*, Apr. 2012.

[22] Kenway, G. K.; Martins, J. R. R. A.: *High-Fidelity Aerostructural Otimization Considering Buffet Onset*. In: *16th AIAA/ISSMO Multidisciplinary Anal-*

ysis and Optimization Conference, American Institute of Aeronautics and Astronauticss, June 2015.

[23] Wrenn, G. A.: *An Indirect Method for Numerical Optimization Using the Kreisselmeier-Steinhauser Function*. Technical Report NAS 1.26:4220. NASA, Jan. 1989.

[24] Chang, K. J.: *Optimality criteria methods using K-S functions*: Structural optimization Nr. 3, P.: 213–217, Sept. 1992.

[25] Abu-Zurayk, M.; Ilić, Č.; Schuster, A.; Liepelt, R.: *Effect of gradient approximations on aero-structural gradient-based wing optimization*. In: EUROGEN 2017. *EUROGEN2017*, 2017.

[26] Klimmek, T.: *Statische aeroelastische Anforderungen beim multidisziplinären Strukturentwurf von Transportflugzeugflügeln*. tech. rep. Göttingen: DLR Institut für Aeroelastik, Aug. 2016.

[27] Gerhold, T.: *Overview of the Hybrid RANS Code TAU*. In: *MEGAFLOW - Numerical Flow Simulation for Aircraft Design*, Springer Berlin Heidelberg, P.: 81–92, 2005.

[28] Ilić, Č.; Abu-Zurayk, M.; Keye, S.; Merle, A.: *Comparison of optimizer-based and flow solver-based trimming in the context of high-fidelity aerodynamic optimization*. In: *20. DGLR-Fach-Symposium der STAB 2016*, P.: 120–121, Nov. 2016.

[29] Vassberg, J.; Dehaan, M.; Rivers, M.; Wahls, R.: *Development of a Common Research Model for Applied CFD Validation Studies*. In: *26th AIAA Applied Aerodynamics Conference*, American Institute of Aeronautics and Astronautics, Aug. 2008.

[30] Rivers, M.; Dittberner, A.: *Experimental Investigations of the NASA Common Research Model in the NASA Langley National Transonic Facility and NASA Ames 11-Ft Transonic Wind Tunnel (Invited)*. In: *49th AIAA Aerospace Sciences Meeting including the New Horizons Forum and Aerospace Exposition*, American Institute of Aeronautics and Astronautics, Jan. 2011.

[31] Koga, S.; Kohzai, M.; Ueno, M.; Nakakita, K.; Sudani, N.: *Analysis of NASA Common Research Model Dynamic Data in JAXA Wind Tunnel Tests*. In: *51st AIAA Aerospace Sciences Meeting including the New Horizons Forum and Aerospace Exposition*, American Institute of Aeronautics and Astronautics, Jan. 2013.

[32] Ueno, M.; Kohzai, M.; Koga, S.; Kato, H.; Nakakita, K.; Sudani, N.: *80% Scaled NASA Common Research Model Wind Tunnel Test of JAXA at Relatively Low Reynolds Number*. In: *51st AIAA Aerospace Sciences Meeting including the New Horizons Forum and Aerospace Exposition*, American Institute of Aeronautics and Astronautics, Jan. 2013.

[33] Rivers, M.; Quest, J.; Rudnik, R.: *Comparison of the NASA Common Research Model European Transonic Wind Tunnel test data to NASA National Transonic Facility test data*: CEAS Aeronautical Journal, July 2017.

[34] Zilliac, G.; Pulliam, T.; Rivers, M.; Zerr, J.; Delgado, M.; Halcomb, N.; Lee, H.: *A Comparison of the Measured and Computed Skin Friction Distribution on the Common Research Model*. In: *49th AIAA Aerospace Sciences Meeting including the New Horizons Forum and Aerospace Exposition*, American Institute of Aeronautics and Astronautics, Jan. 2011.

[35] Keye, S.; Togiti, V.; Eisfeld, B.; Brodersen, O.; Rivers, M.: *Investigation of Fluid-Structure-Coupling and Turbulence Model Effects on the DLR Results of the Fifth AIAA CFD Drag Prediction Workshop*. In: 31st AIAA Applied Aerodynamics Conference. *31st AIAA Applied Aerodynamics Conference*, June 2013.

[36] Keye, S.; Brodersen, O.; Rivers, M. B.: *Investigation of Aeroelastic Effects on the NASA Common Research Model*: Journal of Aircraft Nr. 4, American Institute of Aeronautics and Astronautics (AIAA), P.: 1323–1330, July 2014.

[37] Lyu, Z.; Kenway, G. K.; Martins, J. R. R. A.: *RANS-based Aerodynamic Shape Optimization Investigations of the Common Research Model Wing*. In: *52nd Aerospace Sciences Meeting*, American Institute of Aeronautics and Astronautics, Jan. 2014.

[38] Chen, S.; Lyu, Z.; Kenway, G. K.; Martins, J.: *Aerodynamic Shape Optimization of the Common Research Model Wing-Body-Tail Configuration*. In: *53rd AIAA Aerospace Sciences Meeting*, American Institute of Aeronautics and Astronautics, Jan. 2015.

[39] Kenway, G. K.; Burdette, D. A.; Martins, J.: *Multipoint Aerodynamic Shape Optimization Investigations of the Common Research Model Wing*. In: *53rd AIAA Aerospace Sciences Meeting*, American Institute of Aeronautics and Astronautics, Jan. 2015.

[40] Dunning, P. D.; Stanford, B.; Kim, H. A.: *Aerostructural Level Set Topology Optimization for a Common Research Model Wing*. In: *10th AIAA Multidisciplinary Design Optimization Conference*, American Institute of Aeronautics and Astronautics, Jan. 2014.

[41] Jutte, C. V.; Stanford, B.; Wieseman, C. D.; Moore, J. B.: *Aeroelastic Tailoring of the NASA Common Research Model via Novel Material and Structural Configurations*. In: *52nd Aerospace Sciences Meeting*, American Institute of Aeronautics and Astronautics, Jan. 2014.

[42] Sederberg, T. W.; Parry, S. R.: *Free-form Deformation of Solid Geometric Models*. New York, NY, USA: SIGGRAPH Comput. Graph. Nr. 4, ACM, P.: 151–160, Aug. 1986.